The Astronomical Journal, 154:133 (9pp), 2017 October https://doi.org/10.3847/1538-3881/aa859a

OGLE-2016-BLG-0263Lb: Microlensing Detection of a Very Low-mass Binary Companion through a Repeating Event Channel

C. Han[1], A. Udalski[2,23], A. Gould[3,4,5,24], I. A. Bond[6,25],
and
M. D. Albrow[7], S.-J. Chung[3,8], Y. K. Jung[9], Y.-H. Ryu[3], I.-G. Shin[9], J. C. Yee[9], W. Zhu[4], S.-M. Cha[3,10], S.-L. Kim[3,8], D.-J. Kim[3], C.-U. Lee[3,8], Y. Lee[3,10], B.-G. Park[3,8]
(The KMTNet Collaboration),
J. Skowron[2], P. Mróz[2], P. Pietrukowicz[2], S. Kozłowski[2], R. Poleski[2,4], M. K. Szymański[2], I. Soszyński[2], K. Ulaczyk[2], M. Pawlak[2]
(The OGLE Collaboration),
F. Abe[11], Y. Asakura[11], R. Barry[12], D. P. Bennett[12,13], A. Bhattacharya[12,13], M. Donachie[14], P. Evans[14], A. Fukui[15], Y. Hirao[16], Y. Itow[11], N. Koshimoto[16], M. C. A. Li[14], C. H. Ling[3], K. Masuda[11], Y. Matsubara[11], Y. Muraki[11], M. Nagakane[16], K. Ohnishi[17], C. Ranc[12], N. J. Rattenbury[14], To. Saito[18], A. Sharan[14], D. J. Sullivan[19], T. Sumi[16], D. Suzuki[12,20], P. J. Tristram[21], T. Yamada[22], T. Yamada[16], and A. Yonehara[22]
(The MOA Collaboration)

[1] Department of Physics, Chungbuk National University, Cheongju 28644, Korea
[2] Warsaw University Observatory, Al. Ujazdowskie 4, 00-478 Warszawa, Poland
[3] Korea Astronomy and Space Science Institute, Daejon 34055, Korea
[4] Department of Astronomy, Ohio State University, 140 W. 18th Ave., Columbus, OH 43210, USA
[5] Max Planck Institute for Astronomy, Königstuhl 17, D-69117 Heidelberg, Germany
[6] Institute of Natural and Mathematical Sciences, Massey University, Auckland 0745, New Zealand
[7] University of Canterbury, Department of Physics and Astronomy, Private Bag 4800, Christchurch 8020, New Zealand
[8] Korea University of Science and Technology, 217 Gajeong-ro, Yuseong-gu, Daejeon 34113, Korea
[9] Smithsonian Astrophysical Observatory, 60 Garden St., Cambridge, MA 02138, USA
[10] School of Space Research, Kyung Hee University, Yongin 17104, Korea
[11] Institute for Space-Earth Environmental Research, Nagoya University, Nagoya 464-8601, Japan
[12] Code 667, NASA Goddard Space Flight Center, Greenbelt, MD 20771, USA
[13] Department of Physics, University of Notre Dame, Notre Dame, IN 46556, USA
[14] Department of Physics, University of Auckland, Private Bag 92019, Auckland, New Zealand
[15] Okayama Astrophysical Observatory, National Astronomical Observatory of Japan, 3037-5 Honjo, Kamogata, Asakuchi, Okayama 719-0232, Japan
[16] Department of Earth and Space Science, Graduate School of Science, Osaka University, Toyonaka, Osaka 560-0043, Japan
[17] Nagano National College of Technology, Nagano 381-8550, Japan
[18] Tokyo Metropolitan College of Aeronautics, Tokyo 116-8523, Japan
[19] School of Chemical and Physical Sciences, Victoria University, Wellington, New Zealand
[20] Institute of Space and Astronautical Science, Japan Aerospace Exploration Agency, Kanagawa 252-5210, Japan
[21] University of Canterbury Mt. John Observatory, P.O. Box 56, Lake Tekapo 8770, New Zealand
[22] Department of Physics, Faculty of Science, Kyoto Sangyo University, 603-8555 Kyoto, Japan
Received 2017 May 2; revised 2017 August 7; accepted 2017 August 8; published 2017 September 5

Abstract

We report the discovery of a planet-mass companion to the microlens OGLE-2016-BLG-0263L. Unlike most low-mass companions that were detected through perturbations to the smooth and symmetric light curves produced by the primary, the companion was discovered through the channel of a repeating event, in which the companion itself produced its own single-mass light curve after the event produced by the primary had ended. Thanks to the continuous coverage of the second peak by high-cadence surveys, the possibility of the repeating nature due to source binarity is excluded with a 96% confidence level. The mass of the companion estimated by a Bayesian analysis is $M_{\rm p} = 4.1^{+6.5}_{-2.5}\ M_{\rm J}$. The projected primary-companion separation is $a_\perp = 6.5^{+1.3}_{-1.9}$ au. The ratio of the separation to the snow-line distance of $a_\perp/a_{\rm sl} \sim 15.4$ corresponds to the region beyond Neptune, the outermost planet of the solar system. We discuss the importance of high-cadence surveys in expanding the range of microlensing detections of low-mass companions and future space-based microlensing surveys.

Key words: brown dwarfs – gravitational lensing: micro – planetary systems

1. Introduction

A microlensing signal of a very low-mass companion such as a planet is usually a brief perturbation to the smooth and symmetric lensing light curve produced by the single mass of the primary lens. Short durations of perturbations combined with the nonrepeating nature of lensing events imply that microlensing detections of low-mass companions require high-cadence observations. During the first decade of microlensing surveys, when the survey cadence was not sufficiently high to detect short companion signals, lensing experiments achieved

[23] The OGLE Collaboration.
[24] The KMTNet Collaboration.
[25] The MOA Collaboration.

the required observational cadence by employing a strategy in which lensing events were detected by wide-field surveys, and a fraction of these events were monitored using multiple narrow-field telescopes (Gould & Loeb 1992; Udalski et al. 2005; Beaulieu et al. 2006).

Thanks to the instrumental upgrade of existing surveys and the addition of new surveys, the past decade has witnessed a great increase of the observational cadence of lensing surveys. By entering the fourth phase survey experiment, the Optical Gravitational Lensing Experiment (OGLE) group substantially increased the observational cadence by broadening the field of view (FOV) of their camera from 0.4 $\deg^2$ to 1.4 $\deg^2$ (Udalski et al. 2015). In addition, the Korea Microlensing Telescope Network (KMTNet) group started a microlensing survey in 2015 using three globally distributed telescopes, each of which is equipped with a camera having 4 $\deg^2$ FOV (Kim et al. 2016). Furthermore, the Microlensing Observation in Astrophysics (MOA) group (Bond et al. 2001; Sumi et al. 2003) plans to add a new infrared telescope (T. Sumi 2017, private communication) into the survey. With the elevated sampling rate, microlensing surveys have become increasingly capable of detecting short signals without the need for follow-up observations, e.g., OGLE-2012-BLG-0406Lb (Poleski et al. 2014b), OGLE-2015-BLG-0051/KMT-2015-BLG-0048Lb (Han et al. 2016), OGLE-2016-BLG-0954Lb (Shin et al. 2016), and OGLE-2016-BLG-0596Lb (Mróz et al. 2017).

One very important merit of high-cadence microlensing surveys is the increased rate of detecting very low-mass companions. Currently, more than 2000 lensing events are being detected every season. Due to the limited resources, however, only a handful of events can be monitored by follow-up observations. In principle, follow-up observations can be started at the early stage of anomalies, but implementing this strategy in practice is challenging due to the difficulty in detecting short anomalies in their early stages. By contrast, high-cadence surveys are capable of continuously and densely sampling the light curves of all microlensing events, and thus the rate of detecting very low-mass companions is expected to be greatly increased.

Another important advantage of high-cadence surveys is that they open an additional channel of detecting very low-mass companions. By definition, under the survey+follow-up strategy, events can only be densely monitored by follow-up observations once they have been alerted by surveys. Furthermore, follow-up resources are limited, so in practice those observations have been confined to those located in the narrow region of separations from the host star, the so-called "lensing zone" (Gould & Loeb 1992; Griest & Safizadeh 1998). In contrast, high-cadence surveys are able to densely monitor events not only during the lensing magnification but also before and after it, and this allows low-mass companions to be detected via the "repeating-event" channel. The signal through the repeating-event channel is produced by a companion with a projected separation that is substantially larger than the Einstein radius of the primary star, and it occurs when the source trajectory passes the effective magnification regions of both the primary star and the companion (Di Stefano & Scalzo 1999). Thus, the two lenses (primary and companion) act essentially independently and appear to give rise to two separate microlensing events with different timescales (related by the square root of their mass ratio) but the same source star. Therefore, the channel is important because it expands the region of microlensing detections of low-mass companions to larger separations. Under the assumption of power-law distributions of host-planet separations, Han (2007) estimated that planets detectable by high-cadence surveys through the repeating channel will comprise ∼3%–4% of all planets.

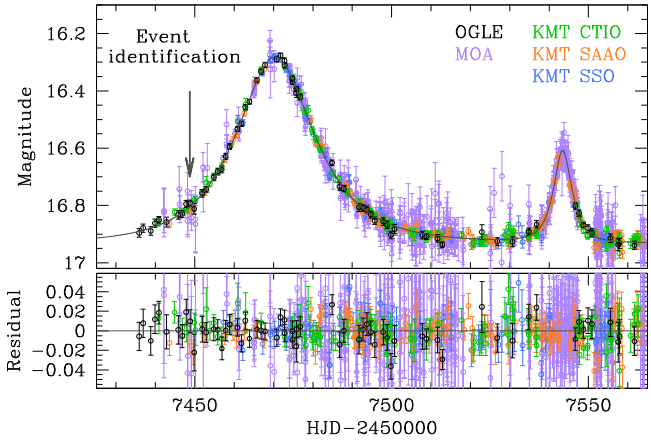

Figure 1. Light curve of OGLE-2016-BLG-0263. The curve superposed on the data points represents the best-fit binary-lens model. The arrow denotes the time when the event was first discovered. The lower panel shows the residual from the model.

In this paper, we report the discovery of a planet-mass binary companion through the repeating-event channel. In Section 2, we describe the survey observations that led to the discovery of the companion. In Section 3, we explain the procedure of analyzing the observed lensing light curve and present the physical parameters of the lens system. We discuss the importance of the repeating-event channel in Section 4.

2. Observation and Data

The low-mass binary companion was discovered from the observation of the microlensing event OGLE-2016-BLG-0263. In Figure 1, we present the light curve of the event. The event occurred on a star located toward the Galactic bulge field with equatorial coordinates $(\mathrm{R.A.}, \mathrm{decl.})_{J2000} = (17^\circ 59' 34\farcs 9, -31^\mathrm{h} 49^\mathrm{m} 07\fs 0)$ that are equivalent to the Galactic coordinates $(l, b) = (-0\fdg 95, -4\fdg 06)$. The lensing-induced brightening of the source star was identified on 2016 March 1 (HJD′ = HJD − 2450000 = 7448.7) by the Early Warning System of the OGLE survey (Udalski et al. 1994; Udalski 2003) using the 1.3 m Warsaw telescope at the Las Campanas Observatory in Chile. Observations by the OGLE survey were conducted with an ∼1 day cadence, and most images were taken in the standard Cousins I band with occasional observations in the Johnson V band for color measurement. After being identified, the event followed a standard point-source point-lens (PSPL) light curve, peaked at HJD′ ∼ 7470, and gradually returned to the baseline magnitude of $I \sim 16.9$.

However, after returning to baseline, the source began to brighten again. The anomaly was noticed on 2016 May 30 (HJD ∼ 7538) and announced to the microlensing community for possible follow-up observations, although none were conducted. The anomaly, which continued for about 10 days, appears to be an independent PSPL event with a short timescale. The time between the first and second peaks of the light curve is ∼73 days.

The event was also in the footprint of the KMTNet and MOA surveys. The KMTNet survey utilizes three globally distributed 1.6 m telescopes that are located at the Cerro Tololo

Table 1
Error-bar Correction Factors

Data Set	k	$\sigma_{\rm min}$
OGLE	1.452	0.001
MOA	1.212	0.001
KMT (CTIO)	1.204	0.001
KMT (SAAO)	1.806	0.001
KMT (SSO)	1.300	0.001

Interamerican Observatory in Chile (KMTC), the South African Astronomical Observatory in South Africa (KMTS), and the Siding Spring Observatory in Australia (KMTA). Similar to the OGLE observations, most of the KMTNet data were acquired using the standard Cousins I-band filter with occasional V-band observations. The event was in the BLG34 field for which observations were carried out with an ~2.5 hr cadence. The MOA survey uses the 1.6 m telescope located at the Mt. John University Observatory in New Zealand. Data were acquired in a customized R-band filter with a bandwidth corresponding to the sum of the Cousins R and I bands. The event was independently found by the MOA survey and dubbed MOA-2016-BLG-075.

Photometry of the images was conducted using pipelines based on the difference imaging analysis method (Alard & Lupton 1998; Woźniak 2000) and customized by the individual groups: Udalski (2003) for OGLE, Albrow et al. (2009) for KMTNet, and Bond et al. (2001) for MOA. In order to analyze the data sets acquired by different instruments and reduced by different photometry pipelines, we readjust the error bars of the individual data sets. Following the usual procedure described in Yee et al. (2012), we normalize the error bars by

$$\sigma = k(\sigma_0^2 + \sigma_{\rm min}^2)^{1/2}, \quad (1)$$

where σ_0 is the error bar estimated from the photometry pipeline, $\sigma_{\rm min}$ is a term used to adjust error bars for consistency with the scatter of the data set, and k is a normalization factor used to make the χ^2 per degree of freedom unity. The χ^2 value is computed based on the best-fit solution of the lensing parameters obtained from modeling (Section 3). In Table 1, we list the error-bar adjustment factors for the individual data sets. We note that the OGLE data used in our analysis were rereduced for optimal photometry and the error bars were estimated according to the prescription described in Skowron et al. (2016), although one still needs a nonunity ($k \neq 1$) scaling factor to make $\chi^2/{\rm dof} = 1$.

3. Analysis

The light curve of OGLE-2016-BLG-0263 is characterized by two peaks in which the short second one occurred well after the first one. The light curve of such a repeating event can be produced in two cases. The first case is a binary-source (BS) event in which the double peaks are produced when the lens passes close to both components of the source separately, one after another (Griest & Hu 1992; Sazhin & Cherepashchuk 1994; Han & Gould 1997). The other case is a binary-lens (BL) event, where the source approaches both components of a widely separated BL, and the source flux is successively magnified by the individual lens components (Di Stefano & Mao 1996). The degeneracy between BS and BL perturbations was first discussed by Gaudi (1998). In order to investigate the nature of the second peak, we test both the BS and BL interpretations.

3.1. BS Interpretation

The light curve of a repeating BS event is represented by the superposition of the PSPL light curves involved with the individual source stars, i.e.,

$$A_{\rm BS} = \frac{A_1 F_{0,1} + A_2 F_{0,2}}{F_{0,1} + F_{0,2}} = \frac{A_1 + A_2 q_F}{1 + q_F}. \quad (2)$$

Here $F_{0,i}$ represents the baseline fluxes of the individual source components and $q_F = F_{0,2}/F_{0,1}$ is the flux ratio between the source components. The lensing magnification involved with each source component is represented by

$$A_i = \frac{u_i^2 + 2}{u_i(u_i^2+4)^{1/2}}; \qquad u_i = \left[u_{0,i}^2 + \left(\frac{t - t_{0,i}}{t_{\rm E}}\right)^2\right]^{1/2}, \quad (3)$$

where $t_{0,i}$ is the time of the closest lens-source approach, $u_{0,i}$ is the lens-source separation at that moment, and $t_{\rm E}$ is the Einstein timescale. For the basic description of the light curve of a BS event, therefore, one needs six lensing parameters, including $t_{0,1}$, $t_{0,2}$, $u_{0,1}$, $u_{0,2}$, $t_{\rm E}$, and q_F (Hwang et al. 2013). The light curve is then modeled as

$$F_j(t_k) = F_{s,j} A_{\rm BS}(t_k;\, t_{0,1},\, u_{0,1},\, t_{0,2},\, u_{0,2},\, t_{\rm E},\, q_F),\, +F_{b,j}, \quad (4)$$

where $(F_{s,j}, F_{b,j})$ are specified separately for each observatory but there is a single q_F for all observatories using a single band (e.g., the I band).

We model the observed light curve based on the BS parameters. Since the light curve of a BS event varies smoothly with the changes of the lensing parameters, we search for the best-fit parameters by χ^2 minimization using a downhill approach. For the downhill approach, we use the Markov chain Monte Carlo (MCMC) method. We set the initial values of $t_{0,1}$ and $t_{0,2}$ based on the times of the first and second peaks, respectively, while the initial values of $u_{0,1}$ and $u_{0,2}$ are determined based on the peak magnifications of the individual peaks. Since both PSPL curves of the individual peaks share a common timescale,[26] we set the initial value of $t_{\rm E}$ as that estimated based on the PSPL fitting of the light curve with the first peak. The initial value of the flux ratio q_F is guessed based on the values of $u_{0,i}$.

In Table 2, we present the parameters of the best-fit BS solution. Also presented is the ratio of the source flux F_s to that of the blend F_b that is estimated from the OGLE data set. The uncertainties of the lensing parameters are estimated based on the scatter of points on the MCMC chain. According to the solution, the second peak was produced by the lens approaching very close to the second source, which is approximately 30 times fainter than the primary source star. In Figure 2, we present the model light curve (dotted curve) superposed on the observed data points. At first glance, the model appears to describe the overall shape of the second peak. However, careful inspection of the model light curve and the residual reveals that the fit is inadequate not only in the rising and falling parts but also near the peak part of the light curve.

[26] In the Appendix, we discuss the possibility of different timescales due to the orbital motion of the source.

Table 2
Best-fit Binary-source Solution

Parameter	Value
χ^2	2598.8
$t_{0,1}$ (HJD)	2457470.441 ± 0.028
$t_{0,2}$ (HJD)	2457543.426 ± 0.028
$u_{0,1}$	0.646 ± 0.032
$u_{0,2}$	0.095 ± 0.004
$t_{\rm E}$ (days)	15.33 ± 0.50
$q_{F,I}$	0.037 ± 0.002
$q_{F,R}$	0.036 ± 0.002
F_s/F_b	2.452/0.219

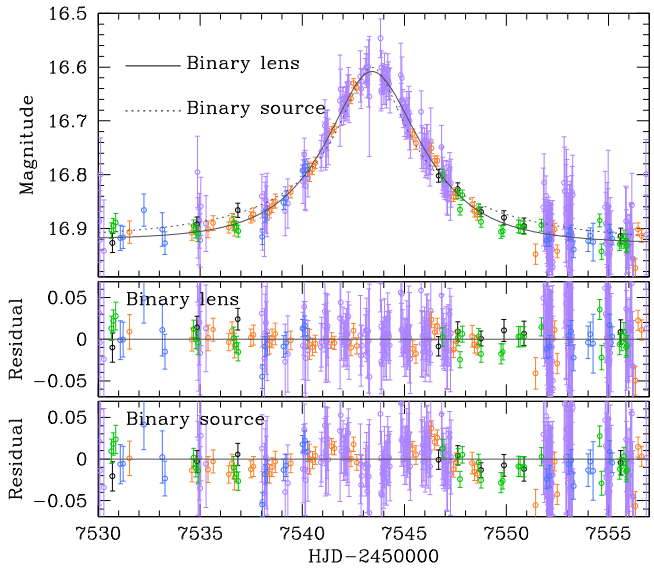

Figure 2. Enlarged view of the light curve around the second peak. Superposed on the data points are the model light curves obtained from binary-lens (solid) and binary-source (dotted) analysis. The lower panels show the residual from the individual models.

We check whether the fit can be further improved with higher-order effects. The trajectory of the lens with respect to the source might deviate from rectilinear due to the orbital motion of the Earth around the Sun. We check this so-called "microlens-parallax" effect (Gould 1992) by conducting additional modeling. Accounting for microlens-parallax effects requires including two additional parameters of $\pi_{{\rm E},N}$ and $\pi_{{\rm E},E}$, which represent the components of the microlens parallax vector $\boldsymbol{\pi}_{\rm E}$ projected onto the sky along the north and east equatorial coordinates, respectively. The direction of $\boldsymbol{\pi}_{\rm E}$ corresponds to that of the relative lens-source motion in the Earth's frame. The magnitude of $\boldsymbol{\pi}_{\rm E}$ is $\pi_{\rm E} = \pi_{\rm rel}/\theta_{\rm E}$, where $\pi_{\rm rel} = {\rm au}(D_{\rm S}^{-1} - D_{\rm L}^{-1})$ is the relative lens-source parallax and $D_{\rm L}$ and $D_{\rm S}$ represent the distances to the lens and source, respectively. From the modeling with parallax effects, we find that the improvement of the fit is very minor with $\Delta\chi^2 \sim 4.4$.

3.2. BL Interpretation

Unlike the case of a BS event, the light curve of a BL event cannot be described by the superposition of the two light curves involved with the individual lens components because the lens binarity induces a region of discontinuous lensing magnifications, i.e., caustics. As a result, the lensing parameters needed to describe a BL event are different from those of a BS event. Basic description of a BL event requires six principal parameters. The first three of these parameters, t_0, u_0, and $t_{\rm E}$, are the same as those of a single-lens event. The other three parameters describe the BL, including the projected separation s (normalized to $\theta_{\rm E}$), the mass ratio q between the binary components, and the angle between the source trajectory and the binary axis, α. Light curves produced by binary lenses are often identified by characteristic spike features that are produced by the source crossings over or approaches close to caustics. In this case, the caustic-involved parts of the light curve are affected by finite-source effects. To account for finite-source effects, one needs an additional parameter, $\rho = \theta_*/\theta_{\rm E}$, where θ_* is the angular source radius. For OGLE-2016-BLG-0263, however, the light curve does not show any feature involved with a caustic, and thus we do not include ρ as a parameter.

Binary lenses form caustics of three topologies (Schneider & Weiss 1986; Erdl & Schneider 1993), which are usually referred to as "close," "resonant," and "wide." For a "resonant" binary, where the projected binary separation is equivalent to the angular Einstein radius, i.e., $s \sim 1$, the caustics form a single big closed curve with six cusps. For a "close" binary with $s < 1 - 3q^{1/2}/4$ (Dominik 1999), the caustic consists of two parts, where one four-cusp caustic is located around the barycenter of the BL and two small three-cusp caustics are positioned away from the barycenter. For a "wide" topology with $s > 1 + 3q^{1/2}/2$ (Dominik 1999), there exist two four-cusp caustics that are located close to the individual lens components.

A repeating BL event is produced by a wide BL, and the individual peaks of the repeating event occur when the source approaches the four-cusp caustics of the wide BL. The caustic has an offset of $\Delta x \sim q/s(1+q)$ with respect to each lens position toward the other lens component (Di Stefano & Mao 1996; An & Han 2002). In the very wide binary regime with $s \gg 1$, each of the two caustics is approximated by the tiny astroidal Chang–Refsdal caustic with an external shear $\gamma = q/[s^2(1+q)]$ (Chang & Refsdal 1984) and the offset $\Delta x \to 0$, implying that the position of the caustic approaches that of the lens components. In this regime, the light curves involved with the individual BL components are described by two separate PSPL curves, and the light curve of the repeating event is approximated by the superposition of the two PSPL curves, i.e., $F_{\rm obs}(t) = F_S[A_1(t) + A_2(t)] + F_b$, where $F_{\rm obs}$ is the observed flux and A_1 and A_2 represent the lensing magnifications involved with the individual lens components. To be noted is that the timescales of the two PSPL curves of a repeating event are proportional to the square root of the masses of the lens components, i.e., $t_{{\rm E},2}/t_{{\rm E},1} = (m_2/m_1)^{1/2} = q^{1/2}$, while the timescales of the two PSPL curves of a repeating BS event are the same because both PSPL curves are produced by a common lens.

To test the BL interpretation, we conduct BL modeling of the observed light curve. Similar to the BS case, we set the initial values of the lensing parameters based on the time of the major peak for t_0, the peak magnification of the major event for u_0, the duration of the major event for $t_{\rm E}$, the ratio of the time gap between the two peaks to the event timescale for $s \sim \Delta t/t_{\rm E}$, the ratio between the timescales of the first and second events for $q \sim (t_{{\rm E},2}/t_{{\rm E},1})^2$, and $\alpha \sim 0$ for a repeating BL event. Based on these initial values, we search for a BL solution using the

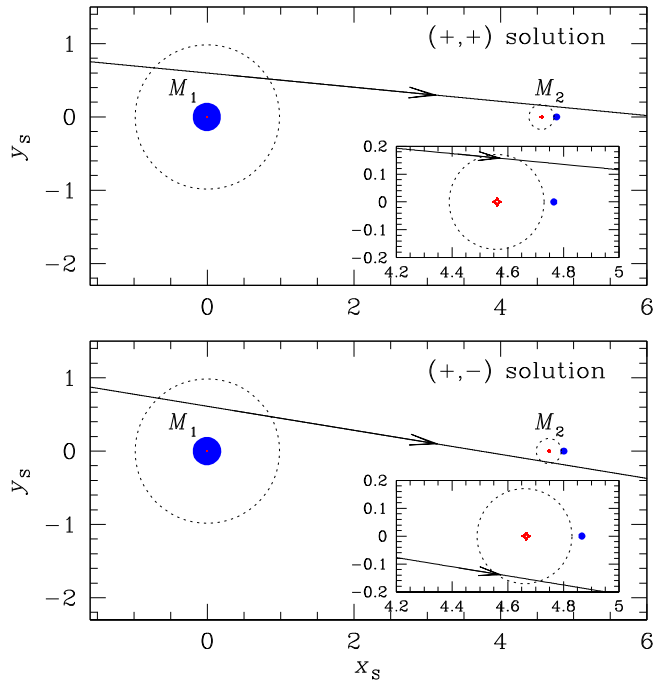

Figure 3. Lens system geometry that shows the source trajectory (line with an arrow) with respect to the binary-lens components (blue dots). Here M_1 and M_2 denote the heavier- and lower-mass components of the binary lens. The dotted circles represent the boundary of effective lensing magnification, and the size of each circle corresponds to the Einstein radius corresponding to the mass of each lens component. The tiny close curves at the centers of the dotted circles represent the caustics. The inset shows the enlarged view of the caustic located close to M_2.

MCMC downhill approach. To double-check the result, we conduct a grid search for a solution in the parameter space of (s, q, α). From this, we confirm that the solution found based on the initial values of the lensing parameters converges with the solution found by the grid search.

Although the binary-lensing model does not suffer from the degeneracy in the s and q parameters, it is found that there exists a degeneracy in the source trajectory angle α. This degeneracy occurs because a pair of solutions with source trajectories passing the lens components on the same, (+, +), solution and the opposite, (+, −), solution sides with respect to the binary axis results in similar light curves (see Figure 3). For OGLE-2016-BLG-0263, we find that the (+, +) solution is slightly preferred over the (+, −) solution by $\Delta\chi^2 = 7.8$.

In Table 3, we present the best-fit BL parameters along with the χ^2 value of the fit. Since the degeneracy between the (+, +) and (+, −) solutions is quite severe, we present both solutions. Because the difference between the source trajectory angles of the two solutions is small, it is found that the lensing parameters of the two solutions are similar to each other. Two factors to be noted are that the binary separation, $s \sim 4.7$, is substantially greater than the Einstein radius and that the mass ratio between the lens components, $q \sim 0.03$, is quite small. We present the model light curve of the best-fit BL solution, i.e., the (+, +) solution, in Figure 1 for the whole event and Figure 2 for the second peak.

In Figure 3, we present the lens system geometry that shows the source trajectory (line with an arrow) with respect to the lens components (blue dots). The upper and lower panels are for the (+, +) and (+, −) solutions, respectively. The tiny red cuspy closed curves near the individual lens components

Table 3
Best-fit Binary-lens Solution

Parameter	(+, +) Solution	(+, −) Solution
χ^2	2438.2	2446.0
t_0 (HJD)	2457470.433 ± 0.036	2457470.432 ± 0.036
u_0	0.581 ± 0.027	0.599 ± 0.031
t_E (days)	16.24 ± 0.45	15.92 ± 0.51
s	4.72 ± 0.12	4.86 ± 0.15
q (10^{-2})	3.06 ± 0.08	2.97 ± 0.09
α (rad)	0.095 ± 0.002	0.163 ± 0.003
F_s/F_b	2.419/0.254	2.543/0.131

represent the caustics. We note that all lengths are scaled to the angular Einstein radius corresponding to the total mass of the BL. The two dotted circles around the individual caustics represent the Einstein rings corresponding to the masses of the individual BL components with radii $r_1 = [1/(1+q)]^{1/2}$ and $r_2 = [q/(1+q)]^{1/2}$. From the geometry, one finds that the source trajectory approached both lens components and the two peaks in the lensing light curve were produced at the moments when the source approached the caustics near the individual lens components. In the regime with a small mass ratio, $q \ll 1$, the caustics located close to the higher- and lower-mass lens components are often referred to as "central" and "planetary" caustics, respectively. The small central caustic is located very close to the higher-mass lens component, and its size as measured by the width along the binary axis is $\sim 4q/(s - s^{-1})^2 \sim 0.006$ (Chung et al. 2005). The comparatively larger planetary caustic is located on the side of the lower-mass lens component with a separation from the heavier lens component of $\sim s - 1/s \sim 4.6$. The size of the planetary caustic is related to the separation and mass ratio of the BL by $\sim 4q^{1/2}/[s(s^2-1)^{1/2}] \sim 0.03$ (Han 2006). Since the distance to each caustic from the source trajectory is much greater than the caustic size, the light curve involved with each lens component appears as a PSPL curve.

3.3. Comparison of Models

Knowing that both BS and BL interpretations can explain the repeating nature of the lensing light curve, we compare the two models in order to find the correct interpretation of the event. For this, we construct the cumulative distribution of the χ^2 difference between the two models.

Figure 4 shows the constructed $\Delta\chi^2$ distribution, where $\Delta\chi^2 = \chi^2_{\rm BS} - \chi^2_{\rm BL}$. The distribution shows that the BL interpretation describes the observed light curve better than the BS interpretation does. The biggest $\Delta\chi^2$ occurs during the second peak. This can also be seen in Figure 2, where the residuals from both models around the second peak are presented. The total χ^2 difference is $\Delta\chi^2 \sim 160$. To show the statistical significance of the difference between the two models, we conduct an F-test for the residuals from the models in the region around the second peak. From this, we find $F = 1.78$. This corresponds to an ~96% probability that the two models have different variances, suggesting that they can be distinguished with a significant confidence level.

We note that the unambiguous discrimination between the two interpretations was possible due to the continuous coverage of the second peak using the globally distributed telescopes. One may note large gaps in the observations from Chile ($7537 < \mathrm{HJD}' < 7546$) and Australia ($7540 < \mathrm{HJD}' < 7551$),

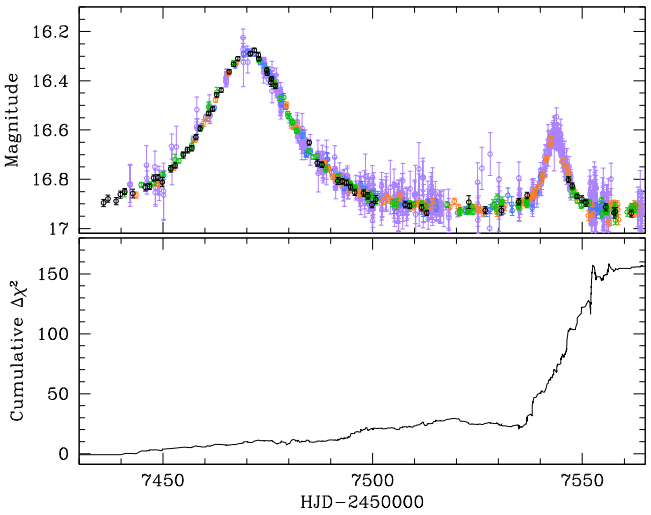

Figure 4. Cumulative distribution of $\Delta\chi^2 = \chi^2_{\rm BS} - \chi^2_{\rm BL}$, where $\chi^2_{\rm BS}$ and $\chi^2_{\rm BL}$ represent the χ^2 values of the binary-source and binary-lens models, respectively.

which were both due to bad weather. Nevertheless, the anomaly was continuously covered by the KMTS and MOA data, enabling accurate interpretation of the event.

Another way to discriminate the BS/BL interpretations is to use color information. This is possible because the colors measured during the two peaks would be different for the BS interpretation, while they should be the same for the BL interpretation. According to the small flux ratio presented in Table 2, the stellar types of the source stars would be greatly different. If a BS interpretation is correct, then the source stars should have significantly different colors. The second peak was observed in the V band by the MOA and KMTNet surveys. In Figure 5, we present the V-band data plotted over the I- and R-band data, showing that the second peak was covered in the V band with six and two points by the MOA and KMTNet surveys, respectively. In the BS modeling, we introduce two flux ratios, $q_{F,I}$ and $q_{F,R}$, to check the possibility of measuring the color difference between the source stars, i.e., $\Delta(R-I) = (R-I)_1 - (R-I)_2 = 2.5\log(q_{F,I}/q_{F,R})$. We note that the R-band flux ratio is measured based on the MOA data. From this, we find $q_{F,I} = 0.037 \pm 0.02$ and $q_{F,R} = 0.036 \pm 0.02$, indicating no color change within the error bar. This suggests the inconsistency in the BS interpretation and further supports the BL interpretation.

3.4. Source Star

Characterizing the source star of a lensing event is important for caustic-crossing BL events because the angular source radius θ_* combined with the normalized source radius ρ enables one to determine the angular Einstein radius, i.e., $\theta_{\rm E} = \theta_*/\rho$. Although one cannot determine $\theta_{\rm E}$ for OGLE-2016-BLG-0263 because the source did not cross caustics and thus the light curve is not affected by finite-source effects, we characterize the source star for the sake of completeness.

The source star is characterized based on its dereddened color $(V-I)_0$ and brightness I_0. We determine the $(V-I)_0$ and I_0 of the source star using the usual method of Yoo et al. (2004), where the instrumental color and brightness of the source are calibrated using the position of the giant clump (GC) centroid, for which the dereddened color and brightness

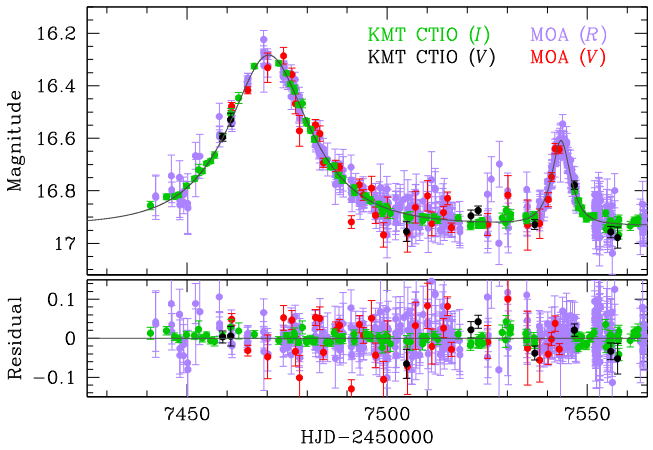

Figure 5. The V-band data from the MOA and KMTNet surveys.

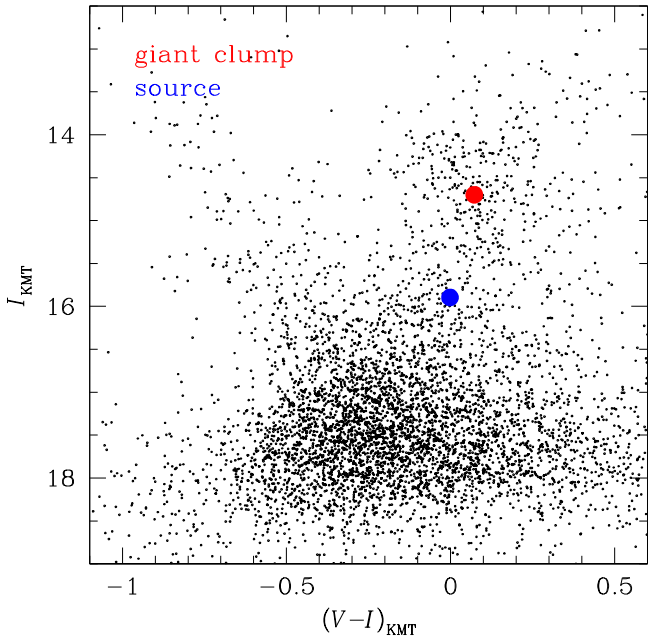

Figure 6. Position of the source star with respect to the centroid of the giant clump in the instrumental color–magnitude diagram of stars in the neighboring region around the source.

$(V-I, I)_{0,\rm GC} = (1.06, 14.63)$ (Bensby et al. 2011; Nataf et al. 2013) are known.

Figure 6 shows the position of the source star with respect to the GC centroid in the instrumental color–magnitude diagram of stars in the $205'' \times 205''$ image stamp centered at the source position. The locations of the source and GC centroid are $(V-I) = (-0.07, 15.89)$ and $(V-I)_{\rm GC} = (0.07, 14.70)$, respectively. From the offsets in color $\Delta(V-I) = (V-I) - (V-I)_{\rm GC} = -0.14$ and magnitude $\Delta I = I - I_{\rm GC} = 1.19$, we estimate that the rereddened color and magnitude of the source star are $(V-I, I)_0 = (0.99, 15.82)$. This indicates that the source is a K-type giant star.

3.5. Physical Parameters

For the unique determination of the mass M and distance $D_{\rm L}$ to the lens, one needs to measure both the microlens parallax $\pi_{\rm E}$ and the angular Einstein radius $\theta_{\rm E}$ that are related to M and $D_{\rm L}$

by

$$M = \frac{\theta_{\rm E}}{\kappa \pi_{\rm E}}; \qquad D_{\rm L} = \frac{\rm au}{\pi_{\rm E}\theta_{\rm E} + \pi_{\rm S}}, \tag{5}$$

where $\kappa \equiv 4G/(c^2\ {\rm au}) \simeq 8.144\ {\rm mas}\ M_\odot^{-1}$ and $\pi_{\rm S}$ denotes the source parallax. For OGLE-2016-BLG-0263, none of these quantities is measured, and thus the physical parameters cannot be uniquely determined. However, one can still statistically constrain the physical lens parameters based on the measured event timescale $t_{\rm E}$ that is related to the physical parameters by

$$t_{\rm E} = \frac{(\kappa M \pi_{\rm rel})^{1/2}}{\mu}; \ \pi_{\rm rel} = {\rm au}\left(\frac{1}{D_{\rm L}} - \frac{1}{D_{\rm S}}\right), \tag{6}$$

where μ represents the relative lens-source proper motion.

In order to estimate the mass and distance to the lens, we conduct a Bayesian analysis of the event based on the measured event timescale combined with the mass function of lens objects and the models of the physical and dynamical distributions of objects in the Galaxy. We use the initial mass function of Chabrier (2003a) for the mass function of Galactic bulge objects and the present-day mass function of Chabrier (2003b) for disk objects. We note that the adopted mass functions extend to substellar objects down to 0.01 $M_\odot$.

For the matter density distribution, we adopt the Galactic model of Han & Gould (2003), where the matter density distribution is constructed based on a double-exponential disk and a triaxial bulge. The velocity distribution is constructed based on the Han & Gould (1995) model, where the disk velocity distribution is assumed to be Gaussian about the rotation velocity of the disk, and the bulge velocity distribution is modeled to be a triaxial Gaussian with velocity components deduced from the flattening of the bulge via the tensor virial theorem. Based on the models, we generate a large number of artificial events by conducting a Monte Carlo simulation. We then estimate the ranges of M and $D_{\rm L}$ corresponding to the measured event timescale.

In Figure 7, we present the probability distributions of the lens mass (upper panel) and distance to the lens (lower panel) obtained from the Bayesian analysis. In Table 4, we present the estimated masses of the individual lens components, M_1 and M_2, the distance to the lens, $D_{\rm L}$, and the projected separation between the lens components, $a_\perp$. We choose the median values of the distributions as representative values, and the uncertainties of the physical parameters are estimated based on the upper and lower boundaries, within which 68% (1σ) of the distribution is encompassed.

The estimated mass of the primary lens is $M_{\rm l} = 0.13^{+0.21}_{-0.08}\ M_\odot$. The central value corresponds to a low-mass M dwarf, which is the most common lens population. The mass of the companion is $M_2 = 4.1^{+6.5}_{-2.5}\ M_{\rm J}$. The upper limit, i.e., $\sim$10.6 $M_{\rm J}$, is below the deuterium-burning limit of $\sim$13 $M_{\rm J}$, indicating that the companion is likely to be a planet. The projected separation between the lens components is $a_\perp = 5.4^{+1.1}_{-1.6}$ au. Under the assumption that the snow line, which separates regions of rocky planet formation from regions of icy planet formation, scales with the mass of a star (Kennedy & Kenyon 2008), the snow line of the host star is $a_{\rm sl} = 2.7\ {\rm au}(M/M_\odot) \sim 0.35$ au, where 2.7 au is the snow line in the solar system (Abe et al. 2000; Rivkin et al. 2002). If the companion is a planet, then the ratio of the M_1–M_2 separation to the snow-line distance of the planetary system is $a_\perp/a_{\rm sl} \sim 15.4$. This ratio corresponds to the region beyond Neptune, the outermost planet of the solar system.

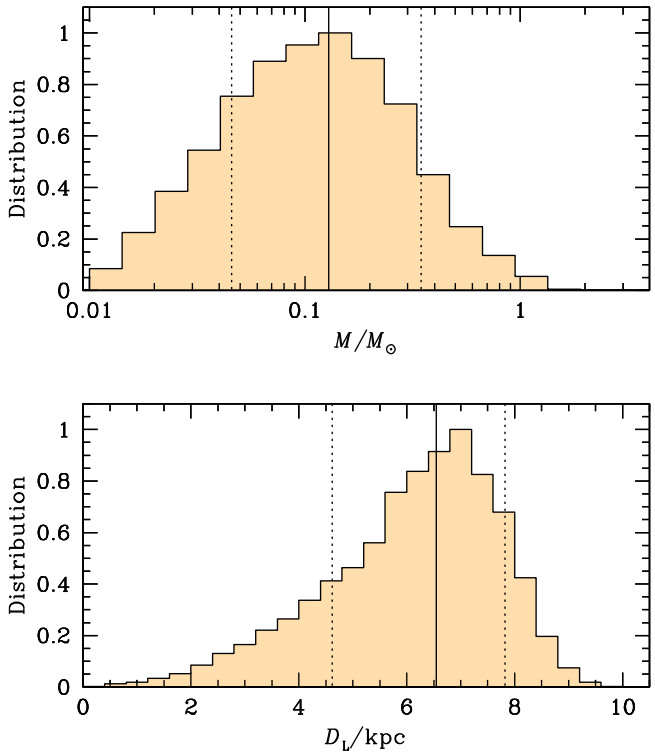

Figure 7. Distributions of the lens mass (upper panel) and distance to the lens (lower panel) estimated by Bayesian analysis. The solid vertical line in each panel denotes the median value, and the region enclosed by the dotted lines represents the 1σ (68%) range of the distribution.

Table 4
Physical Parameters

Parameter	Value
Mass of the primary (M_1)	$0.13^{+0.21}_{-0.08}\ M_\odot$
Mass of the companion (M_2)	$4.1^{+6.5}_{-2.5}\ M_{\rm J}$
Distance to the lens ($D_{\rm L}$)	$6.5^{+1.3}_{-1.9}$ kpc
Projected separation ($a_\perp$)	$5.4^{+1.1}_{-1.6}$ au

4. Discussion

The discovery of OGLE-2016-BLG-0263LB demonstrates that high-cadence surveys can provide an additional channel for detecting very low-mass companions through repeating events. The scientific importance of the repeating-event channel is that the range of planets and brown dwarfs (BDs) detectable by microlensing is expanded.

The usefulness of the repeating-event channel is illustrated in Figure 8, where we plot the position of OGLE-2016-BLG-0263LB among the 48 previously discovered microlensing planets in the q–s parameter space. In the plot, filled circles represent planets for which the lensing parameters are unambiguous determined. Open circles represent planets for which the solutions suffer from degeneracy, mostly by the well-known close/wide degeneracy between the solutions with s and s^{-1} (Griest & Safizadeh 1998). In this case, we mark both solutions. From the locations of planets, it is found that most planets are concentrated in the region around $s = 1.0$ (Mróz et al. 2017) because they were detected from the anomalies that

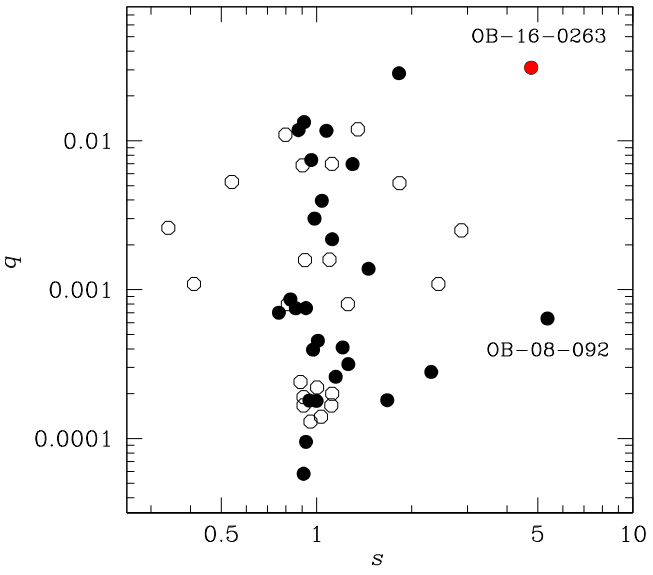

Figure 8. Plot of planet–star separation s vs. the mass ratio q of 48 previously discovered microlensing planets. The filled circles represent planets for which the lensing parameters are uniquely determined, while the open circles represent planets with close/wide degeneracy. For the planets suffering from the degeneracy, we mark two points with s and s^{-1}. The red circle denotes OGLE-2016-BLG-0263Lb, reported in this work.

occurred during the lensing magnification by their host stars. By contrast, OGLE-2016-BLG-0263LB is located in the unpopulated region of wide separations. It has the largest separation after OGLE-2008-BLG-092LAb, which has a projected separation from its host of $s \sim 5.3$ (Poleski et al. 2014a). We note that OGLE-2008-BLG-092LAb was also detected through the repeating-event channel.

The repeating-event channel is also important in future space-based microlensing surveys, such as *WFIRST*, from which many free-floating planet candidates are expected to be detected. Microlensing events produced by free-floating planets appear as short-timescale events. However, bound planets with large separations from their host stars can also produce similar signals, masquerading as free-floating planets (Han et al. 2005). High-cadence ground-based surveys are important because they enable us to distinguish some bound planets from free-floating planets through the repeating-event channel. Due to the time-window limit set by the orbits of satellites, space-based lensing observations will not observe the bulge field continuously. For example, the *WFIRST* survey is planned to be conducted for ∼70 days each season. With the data obtained from space observations, then, it will be difficult to sort out short-timescale events produced by bound planets through the repeating-event channel. In contrast, ground-based surveys continue for much longer periods, ∼8 months on average, and thus they can provide an important channel to filter out bound planets from the sample of free-floating planet candidates.

Work by C.H. was supported by grant 2017R1A4A1015178 of the National Research Foundation of Korea. The OGLE project has received funding from the National Science Centre, Poland, grant MAESTRO 2014/14/A/ST9/00121 to A. Udalski. The OGLE Team thanks Profs. M. Kubiak, G. Pietrzyński, and Ł. Wyrzykowski for their contribution to the collection of the OGLE photometric data. This research has made use of the KMTNet system operated by the Korea Astronomy and Space Science Institute (KASI), and the data were obtained at three host sites of CTIO in Chile, SAAO in South Africa, and SSO in Australia. Work by A.G. was supported by JPL grant 1500811. A.G. and W.Z. acknowledge the support of NSF grant AST-1516842. Work by J.C.Y. was performed under contract with the California Institute of Technology (Caltech)/Jet Propulsion Laboratory (JPL) funded by NASA through the Sagan Fellowship Program executed by the NASA Exoplanet Science Institute. We acknowledge the high-speed internet service (KREONET) provided by the Korea Institute of Science and Technology Information (KISTI).

Appendix

In the usual investigation of BS solutions for which the two components are well separated, the components are treated as having fixed separation. Hence, in this approximation, the two well-separated events are treated as having a single Einstein timescale $t_{\rm E}$. Indeed, this is one of the principal characteristics used to distinguish BS and BL models: if the timescales differ, it implies a BL with mass ratio $q = (t_{\rm E,2}/t_{\rm E,1})^2$.

Nevertheless, at some level, the two components must be moving, so the Einstein timescales cannot be strictly equal. Here we quantify what level of difference is plausible. Of course, it is known that binary orbital motion can give rise to significant light-curve variations (Han & Gould 1997), and these can, in principle, be quite complicated. However, here we are working in the wide-separation limit and so will take a perturbative approach, defined by

$$\epsilon \equiv \frac{\Delta t_{\rm E}}{t_{\rm E}};\ \Delta t_{\rm E} \equiv t_{\rm E,2} - t_{\rm E,1}. \tag{7}$$

Since the components are well-separated, $\Delta t_{\rm E}$ is sensitive only to motion along the direction of projected separation,

$$\begin{aligned}\Delta v_{s,\parallel} &= D_s(\mu_{s,2,\parallel} - \mu_{s,1,\parallel}) \\ &= D_s\left(\frac{\theta_{\rm E}}{t_{\rm E,2}} - \frac{\theta_{\rm E}}{t_{\rm E,1}}\right) \simeq -\frac{D_s\theta_{\rm E}\Delta t_{\rm E}}{t_{\rm E}^2}.\end{aligned} \tag{8}$$

The projected physical separation between the components is

$$\begin{aligned}a_\perp &= D_s\mu_{\rm rel}\Delta t_0 = D_s\theta_{\rm E}\frac{\Delta t_0}{t_{\rm E}}, \\ \Delta t_0 &\equiv t_{0,2} - t_{0,1}.\end{aligned} \tag{9}$$

Then, for the system to be bound, $v_{s,\parallel}^2 < GM_s/a_\perp$, where M_s is the total mass of the source (typically $M_s \sim 2\,M_\odot$ for two sources visible in the bulge, although this may not hold if one of these repeating events is extremely highly magnified). This can be expressed as

$$1 > \frac{a_\perp v_{s,\parallel}^2}{GM_s} = \left(\frac{D_s\theta_{\rm E}}{t_{\rm E}}\right)^3\frac{\Delta t_0}{GM_s}\epsilon^2, \tag{10}$$

Table 5
Binary-source Solution with Two Timescales

Parameter	Value
$t_{0,1}$ (HJD)	2457470.465 ± 0.040
$t_{0,2}$ (HJD)	2457543.474 ± 0.040
$u_{0,1}$	0.608 ± 0.049
$u_{0,2}$	0.394 ± 0.049
$t_{E,1}$ (days)	15.81 ± 0.82
$t_{E,2}$ (days)	5.05 ± 0.53
q_F	0.225 ± 0.026
F_s/F_b	3.098/−0.424

i.e.,

$$\frac{\theta_E}{\rm mas} < \frac{t_E}{D_s({\rm au/kpc})}\left(\frac{GM_s}{\epsilon^2\Delta t_0}\right)^{1/3} = \frac{t_E\ /{\rm yr}}{D_s/{\rm kpc}}\left(\frac{4\pi^2 M_s/M_\odot}{\epsilon^2\Delta t_0\ /{\rm yr}}\right)^{1/3}. \quad (11)$$

We now apply this formalism to the case of OGLE-2016-BLG-0263. We first search for BS solutions as in Section 3.1 but with the additional degree of freedom $t_E \rightarrow (t_{E,1}, t_{E,2})$. The results in Table 5 show that this model comes close to matching the BL model in terms of χ^2 but at the cost of a radical divergence of Einstein timescales: $(t_{E,1}, t_{E,2}) = (15.8, 5.0)$ days. We note that, in addition, the blending is negative, $F_b = -0.42$, corresponding to an $I = 19$ "anti-star," which would require a "divot" in the stellar background of this amplitude. Negative blending might be caused by either an incorrect model or a fluctuation of data for a small F_b case. Due to the latter possibility, negative blending at this level cannot be excluded.

To apply the formalism, we first note that the flux of the secondary indicates that it is an upper main-sequence star, so the masses of the two sources are $M_{s,1} \simeq M_{s,2} \simeq 1\ M_\odot$. We then adopt $t_E = (t_{E,1}t_{E,2})^{1/2} = 8.9$ days, so that $\epsilon = 1.17$, which is outside the "perturbative regime." Nevertheless, if one carries through the nonperturbative calculation, the final result hardly differs. We obtain

$$\theta_E < 0.02\ {\rm mas};\ \mu < 0.8\ {\rm mas\ yr^{-1}}.$$

The limit on μ would already make the lens quite unusual, though hardly unprecedented. However, the low value of θ_E is more constraining. For example, for typical bulge lenses with D_S–$D_L = 1$ kpc, this would imply a lens mass $M_L < 0.003\ M_\odot$, and for disk lenses, M_L would be even lower. The combination of somewhat low proper motion and very low Einstein radius would make this a very remarkable lens.

Moreover, we note that we have been extraordinarily conservative in putting "1" on the right-hand side of Equation (10). Because we are viewing only one component of motion and very few systems would be seen either face-on or near local escape velocity, we could have chosen a typical value "1/8," rather than a strict upper limit. Thus, a more typical source geometry would yield $\theta_E \sim 0.01$ mas, which would imply $M_L < 0.0007\ M_\odot$,

We conclude that while the data can be well matched to a BS with large internal motion, this requires an improbably small Einstein radius. Hence, in this case, such solutions are highly disfavored.

ORCID iDs

C. Han https://orcid.org/0000-0002-2641-9964
M. D. Albrow https://orcid.org/0000-0003-3316-4012
S.-J. Chung https://orcid.org/0000-0001-6285-4528
Y.-H. Ryu https://orcid.org/0000-0001-9823-2907
J. C. Yee https://orcid.org/0000-0001-9481-7123
J. Skowron https://orcid.org/0000-0002-2335-1730
P. Pietrukowicz https://orcid.org/0000-0002-2339-5899
S. Kozłowski https://orcid.org/0000-0003-4084-880X

References

Abe, Y., Ohtani, E., Okuchi, T., Righter, K., & Drake, M. 2000, in Origin of the Earth and Moon, ed. R. M. Canup & K. Righter (Tucson, AZ: Univ. Arizona Press), 413
Alard, C., & Lupton, R. H. 1998, ApJ, 503, 325
Albrow, M. D., Horne, K., Bramich, D. M., et al. 2009, MNRAS, 397, 2099
An, J. H., & Han, C. 2002, ApJ, 573, 351
Beaulieu, J.-P., Bennett, D. P., Fouqué, P., et al. 2006, Natur, 439, 437
Bensby, T., Adén, D., Meléndez, J., et al. 2011, A&AA, 533, 134
Bond, I. A., Abe, F., Dodd, R. J., et al. 2001, MNRAS, 327, 868
Chabrier, G. 2003a, PASP, 115, 763
Chabrier, G. 2003b, ApJL, 586, L133
Chang, K., & Refsdal, S. 1984, A&A, 132, 168
Chung, S.-J., Han, C., & Park, B.-G. 2005, ApJ, 630, 535
Di Stefano, R., & Mao, S. 1996, ApJ, 457, 93
Di Stefano, R., & Scalzo, R. A. 1999, ApJ, 512, 579
Dominik, M. 1999, A&A, 349, 108
Erdl, H., & Schneider, P. 1993, A&A, 268, 453
Gaudi, B. S. 1998, ApJ, 506, 533
Gould, A. 1992, ApJ, 392, 442
Gould, A., & Loeb, A. 1992, ApJ, 396, 104
Griest, K., & Hu, W. 1992, ApJ, 397, 362
Griest, K., & Safizadeh, N. 1998, ApJ, 500, 37
Han, C. 2006, ApJ, 638, 1080
Han, C. 2007, ApJ, 670, 1361
Han, C., Gaudi, B. S., An, J. H., & Gould, A. 2005, ApJ, 618, 962
Han, C., & Gould, A. 1995, ApJ, 447, 53
Han, C., & Gould, A. 1997, ApJ, 480, 196
Han, C., & Gould, A. 2003, ApJ, 592, 172
Han, C., Udalski, A., Gould, A., et al. 2016, AJ, 152, 95
Hwang, K.-H., Choi, J.-Y., Bond, I. A., et al. 2013, ApJ, 778, 55
Kennedy, G. M., & Kenyon, S. J. 2008, ApJ, 673, 502
Kim, S.-L., Lee, C.-U., Park, B.-G., et al. 2016, JKAS, 49, 37
Mróz, P., Han, C., Udalski, A., et al. 2017, AJ, 153, 143
Nataf, D. M., Gould, A., Fouqué, P., et al. 2013, ApJ, 769, 88
Poleski, R., Skowron, J., Udalski, A., et al. 2014a, ApJ, 795, 42
Poleski, R., Udalski, A., Dong, S., et al. 2014b, ApJ, 782, 47
Rivkin, A. S., Howell, E. S., Vilas, F., & Lebofsky, L. A. 2002, in Asteroids III, ed. W. K. Bottke et al. (Tucson, AZ: Univ. Arizona Press), 235
Sazhin, M. V., & Cherepashchuk, A. M. 1994, AstL, 20, 523
Schneider, P., & Weiss, A. 1986, A&A, 164, 237
Shin, I.-G., Ryu, Y.-H., Udalski, A., et al. 2016, JKAS, 49, 73
Skowron, J., Udalski, A., Kozłowski, S., et al. 2016, AcA, 66, 1
Sumi, T., Abe, F., Bond, I. A., et al. 2003, ApJ, 591, 204
Udalski, A. 2003, AcA, 53, 291
Udalski, A., Jaroszyński, M., Paczyński, B., et al. 2005, ApJL, 628, L109
Udalski, A., Szymański, M., Kałużny, J., et al. 1994, AcA, 44, 227
Udalski, A., Szymański, M. K., & Szymański, G. 2015, AcA, 65, 1
Woźniak, P. R. 2000, AcA, 50, 421
Yee, J. C., Shvartzvald, Y., Gal-Yam, A., et al. 2012, ApJ, 755, 102
Yoo, J., DePoy, D. L., Gal-Yam, A., et al. 2004, ApJ, 603, 139